Ptychography using Blind Multi-Mode PMACE

Qiuchen Zhai, *Student Member, IEEE,* Gregery T. Buzzard, *Senior Member, IEEE,* Kevin Mertes, Brendt Wohlberg, *Fellow, IEEE,* Charles A. Bouman, *Life Fellow, IEEE*

***Abstract*—Ptychography is an imaging technique that enables nanometer-scale reconstruction of complex transmittance images by scanning objects with overlapping X-ray illumination patterns. However, the illumination function is typically unknown and only partially coherent, which presents challenges for reconstruction.**

In this paper, we introduce Blind Multi-Mode Projected Multi-Agent Consensus Equilibrium (BM-PMACE) for blind ptychographic reconstruction. BM-PMACE jointly estimates both the complex transmittance image and the multi-modal probe functions associated with a partially coherent probe source. Importantly, BM-PMACE maintains a location-specific probe state that captures spatially varying probe aberrations. Our method also incorporates a dynamic strategy for integrating additional probe modes. Our experiments on synthetic and measured data demonstrate that BM-PMACE outperforms existing approaches in reconstruction quality and convergence rate.

***Index Terms*—Ptychography, consensus equilibrium, inverse problem, phase retrieval, iterative reconstruction.**

I. Introduction

PTYCHOGRAPHY is a lensless X-ray imaging technique often used for non-destructive X-ray imaging. By using X-ray wavelengths typically in the range of 0.2 to 2 nm, ptychography can achieve nanometer resolution [1]–[5]. Moreover, it can also be combined with advanced imaging modalities, such as tomography [6]–[10], to produce high-resolution images and provide detailed insights into complex nano-scale structures. As a result, ptychography has applications in fields ranging from biomedical imaging [11], [12] to material science [13]–[15].

In ptychography, a sequence of overlapping regions is scanned with a coherent or partially coherent light source known as a probe [16]. At each probe location, the intensity of the resulting diffraction pattern is measured by an imaging detector positioned in the far-field plane. These real-valued diffraction measurements are used to reconstruct the complex transmission image by solving a phase recovery problem. Since the phase is lost in measurement, the forward model for ptychography is non-linear, the reconstruction problem is typically ill-posed, and the associated optimization problems are non-convex and non-smooth [17]. However, the overlapping probe locations provide redundancy in the measurements that make it possible to solve the associated inverse problem. Fourier ptychography is a related computational imaging technique that captures a series of data by illuminating the sample at varying angles [18], [19]. This difference in data acquisition requires distinct reconstruction algorithms from the ptychography considered here.

Accurate reconstruction of the complex transmittance image depends critically on a precise characterization of the light probe [20]–[22]. However, in real-world experiments, the probe function is rarely fully-known, and typically only partially coherent. This partial coherence arises because any vibration, energy spread in the beam, or environmental interference can disrupt the coherence and lead to incoherent wave superposition [23], [24]. Reconstruction from partially coherent data enables the collection of data with higher flux light sources [25] and fly-scan techniques [26]–[28], both of which can reduce acquisition time. However, with partially-coherent data, single-mode ptychographic reconstruction may fail or produce poor results with artifacts [29], [30]. This motivates a form of ptychography known as blind reconstruction, in which the multi-mode complex probe function and the complex transmittance image are estimated jointly [31], [32].

Table I lists several existing ptychographic reconstruction algorithms along with relevant characteristics and qualitative performance. Among the methods that are designed for partially coherent probes, a common approach is to reconstruct multiple mutually non-coherent probe modes using blind multi-mode reconstruction. Ptychographic engine (PIE) [2], [41] and its variants [33], [42], [43], Difference Map (DM) [44], [45], and SHARP [37], [46] use alternating updates of the complex transmittance and the probe function. Both ePIE [34], [47] and DM [36], [48], [49] have been modified to support blind multi-mode reconstruction. The multi-mode ePIE algorithm employs a serial approach in which each probe location is updated in sequence. This has the advantage of speeding per-iteration convergence, since the multi-mode probe estimate is also updated with each image patch update. However, serial update is not practical for large ptychography problems, which may have millions of probe locations [50]. Moreover, gradient-based algorithms such as ePIE can sometimes exhibit slow convergence or become trapped in local minima when the data are noisy and/or sparse [51], [52].

More recent gradient-based frameworks include linear least-squares maximum likelihood (LSQML) and automatic differentiation (AD) methods. LSQML as described in [53], [54] supports a variety of formulations and uses gradient-based methods to approximate the full nonlinear problem with a

The work of Q. Zhai was supported by U.S. Department of Energy through LANL. The work of C. A. Bouman was supported in part by the U.S. Department of Energy and the Showalter Trust. The work of G.T. Buzzard was partially supported by NSF CCF-1763896. The work of B. Wohlberg was supported by the LDRD program of LANL under project number 20200061DR. The publication release number is LA-UR-24-33356.

Qiuchen Zhai and Charles A. Bouman are with the School of Electrical and Computer Engineering, Purdue University, 465 Northwestern Ave., West Lafayette, IN 47907, USA (qzhai@purdue.edu and bouman@purdue.edu).

Gregery T. Buzzard is with the Department of Mathematics, Purdue University, West Lafayette, IN 47907, USA (buzzard@purdue.edu).

Kevin Mertes is with Physical Chemistry and Applied Spectroscopy Group, Los Alamos National Laboratory, Los Alamos, NM 87545 USA (kmmertes@lanl.gov).

Brendt Wohlberg is with CCS-3 Information Sciences Group, Los Alamos National Laboratory, Los Alamos, NM 87545 USA (brendt@lanl.gov).

Algorithm	Type	Blind Recon.	Multi-Mode Probe	Performance on sparse data	Performance on noisy data
ePIE [33], [34]	Serial	Yes	Yes	Fair	Fair
DM [35], [36]	Parallel	Yes	Yes	Good	Good
SHARP [37]	Parallel	Yes	No	Good	Good
WF/AWF [38]	Parallel	No	No	Good	Fair
GDP-RAAR/ADMM [16], [39]	Parallel	Yes	Yes	Good	Good
PMACE [40]	Parallel	No	No	Excellent	Excellent
BM-PMACE [this paper]	Parallel	Yes	Yes	Excellent	Excellent

Table I: Comparison of ptychography reconstruction algorithm features.

linear least-squares (LSQ) optimization. These publications report that LSQML has fast convergence with good reconstruction quality, but it currently does not support multi-mode probe estimation. Reference implementations are available from [55], [56]. Emerging AD methods based on programming languages such as Pytorch or JAX can compute the exact gradient for complex and nonlinear forward models [57]–[61]. However, automatically computed back-propagation algorithms can pose demanding memory and computational overhead requirements for large datasets [62], and they can yield unreliable gradients in regions with sharp discontinuities or near-flat behavior due to floating-point limitations [63]. Moreover, once the gradient is computed, a fast algorithm is required for optimization, which in general depends on the details of the problem being solved.

Alternatively, DM algorithms allow for parallelization and also support blind multi-mode reconstruction. These methods refine the estimate across multiple scan locations simultaneously, resulting in more generalized estimates. This approach improves computational efficiency by leveraging distributed computation and offers better scalability for large-scale datasets. However, parallel methods may require additional iterations to converge compared to serial approaches [64]. More recent algorithms include GDP-RAAR [39] and GDP-ADMM [16]. While both algorithms have been demonstrated to be effective, they both use a non-standard physical model in which the probe convolution occurs after the energy detection. While GDP-RAAR and GDP-ADMM also support parallel processing and blind multi-mode reconstruction, they may not accurately capture the underlying physics. The orthogonal probe relaxation (OPR) method [65], [66] reconstructs a separate probe for each scanning position and links them through low-dimensional subspace projection using SVD. While OPR captures small instabilities across scan locations, it does not model partial coherence of the illumination source.

Finally, Wirtinger flow (WF) [38] and Projected Multi-Agent Consensus Equilibrium (PMACE) [40], [67] have been proposed with a focus on reconstruction of the complex transmittance image, without providing a well-defined strategy for probe estimation. However, despite the lack of probe estimation, the PMACE algorithm has been shown to provide more accurate reconstructions than alternative algorithms when the probe locations are sparse or contain positional errors [40], [67].

In this paper, we introduce Blind Multi-Mode Projected Multi-Agent Consensus Equilibrium (BM-PMACE) for blind ptychographic reconstruction.[1] BM-PMACE jointly estimates both the complex transmittance image and the multi-modal probe functions associated with a partially coherent probe source. Importantly, BM-PMACE maintains a location-specific probe state that captures spatially varying probe aberrations. Moreover, we demonstrate that by keeping local probe estimates for each patch, the BM-PMACE algorithm achieves much faster and more robust per-iteration convergence for blind multi-mode reconstruction with respect to comparison algorithms based on a global probe state.

Since BM-PMACE is based on PMACE, it allows for fast and parallel reconstruction of the transmission image and produces good quality reconstructions with sparse and noisy data. It is also parallelizable for practical application on large data sets.

More specifically, we make the following contributions:

- Formulate the BM-PMACE algorithm for blind multi-mode ptychographic reconstruction based on the PMACE algorithm; Introduce a multi-mode probe estimate based on a distributed state that accounts for local variations in the probe;
- Introduce a method for dynamic addition of probe modes. Introduce a scan position refinement approach for correcting positional errors of recorded scan locations.

Our experimental results on both synthetic and measured ptychography data demonstrate that the distributed probe estimates consistently result in faster and more robust per-iteration convergence and better reconstructed image quality than competing methods.

II. Overview of Blind Multimode Ptychography

Figure 1 illustrates how ptychography is performed. A coherent radiation source, such as soft X-rays or electrons, is used to generate a "probe" that illuminates a series of overlapping patches in a larger flat object. For each probe location, the intensity of the resulting far-field diffraction pattern is measured. The 2D image is then reconstructed by estimating the complex transmittance image as part of a larger phase recovery problem.

To first order, the phase of the reconstructed 2D image changes in proportion to the thickness of the sample and hence

[1] A reference open-source implementation of BM-PMACE is available at https://github.com/cabouman/ptycho_pmace.

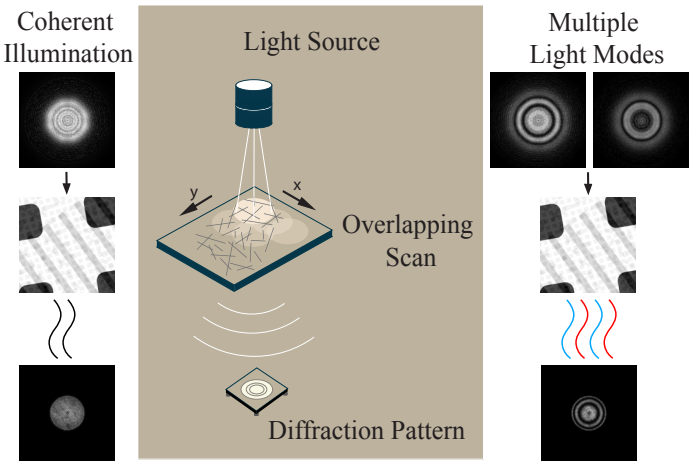

Figure 1: Illustration of ptychography with coherent and partially coherent light sources. On the left, the coherent light source illuminates part of the sample, resulting in a uniform and sharp diffraction pattern. On the right, the partially coherent light source produces a superimposed diffraction pattern.

gives precise information about sample thickness for a known, single-component material. This fact is due to the phase shift induced by the sample, which depends on both its refractive index and thickness.

In blind multi-mode ptychography, we assume that the illumination source is both unknown and partially coherent. In this case, the probe is not fully coherent, so we model the probe as consisting of multiple, mutually incoherent modes. These modes are summed in energy, and a 2D complex probe cross section must be estimated for each mode individually.

A. Notation and Forward Model

We let $x \in \mathbb{C}^{N_1 \times N_2}$ denote the complex transmittance function of the object being imaged, where N_1 and N_2 represent the number of pixels along the horizontal and vertical dimensions of the object. We let $d_k \in \mathbb{C}^{N_p \times N_p}, k \in \{0, \dots, K-1\}$ represent the set of multiple probe modes used to illuminate the sample, where N_p represents the number of pixels along each dimension of the probe mode and K denotes the total number of probe modes. Furthermore, let $D_k = \text{diag}(d_k)$ denote the diagonal matrix representing the complex illumination function of the kth probe mode. Then the forward model of the diffraction pattern from the kth mode of the jth probe location is given by

$$\bar{I}_{j,k} = |\mathcal{F} D_k v_j|^2 = |\mathcal{F} D_k P_j x|^2 \ ,$$

where $P_j : \mathbb{C}^{N_1 \times N_2} \to \mathbb{C}^{N_p \times N_p}$ denotes the linear projection operator that extracts the localized patch associated with jth probe location, $v_j = P_j x$ represents the corresponding patch, D_k multiplies by the complex probe intensity, and $\mathcal{F}$ denotes the 2D orthonormal discrete Fourier Transform. Note that the intensity is proportional to the square of the electric field.

The detector measurements I_j are then Poisson-distributed random variables with means that are proportional to the sum of the energy from all the modes. Since the probe modes are not coherently related, the phases are relatively random and the modes are additive in energy. Consequently, we have that

$$\begin{aligned} I_j &= \text{Pois}\left(\sum_{k=0}^{K-1} \bar{I}_{j,k}\right) \\ &= \text{Pois}\left(\sum_{k=0}^{K-1} |\mathcal{F} D_k v_j|^2\right) \ , \end{aligned} \tag{1}$$

where $\text{Pois}(\lambda)$ denotes an array of independent Poisson distributed random variables with means parameterized by the array λ. We note that GDP-RAAR [39] and GDP-ADMM [16] make the approximation of interchanging the non-linear operator $|\cdot|^2$ and the linear operator D_k.

While some methods directly process the Poisson measurements [68], we apply a variance-stabilizing transformation to the detector measurements by taking the square root [69]. Therefore, the forward model for our multi-mode ptychography system is given by

$$y_j = \sqrt{\text{Pois}\left(\sum_{k=0}^{K-1} |\mathcal{F} D_k v_j|^2\right)} \ . \tag{2}$$

This transformation simplifies the forward model of our approach.

In the following sections, we extend the PMACE framework of [40], [67] to the case of blind multi-mode reconstruction of ptychography data. To do this, we first derive the PMACE algorithm for non-blind multi-mode reconstruction in Section III. We then derive the corresponding algorithms for PMACE reconstruction of the probe modes in Section IV. Finally, in Section V we introduce an integrated algorithm for blind, multi-mode PMACE (BM-PMACE) reconstruction.

III. Image Reconstruction using PMACE

In this section, we derive a PMACE algorithm for multi-mode reconstruction of the transmission image x, assuming that we know the probe modes, d_k, $k = 0, \dots K-1$. We discuss probe estimation in Section IV-B.

Figure 2 illustrates the PMACE pipeline for object refinement and gives a conceptual overview of how the complex transmittance image, patch estimates, data-fitting agents, and the pixel-weighted averaging operator interact to drive the iterative reconstruction process. We give more detail below, but roughly, each patch represents a local region of the object, and updates are performed individually by the agent $F_j^I(\cdot)$ to refine the complex transmittance patches based on the measured diffraction patterns. The pixel-averaging operator $\mathbf{G}^I(\cdot)$ enforces agreement between overlapping patches by averaging the estimates from the agents.

A. Image Update Pipeline

To specify the image update algorithm, recall that P_j is a linear operator that extracts the jth patch from the image x. We can then stack these patch states $v_j = P_j x$ into a larger collection given by

$$\mathbf{v} = [v_0, \dots, v_{J-1}]^t \ . \tag{3}$$

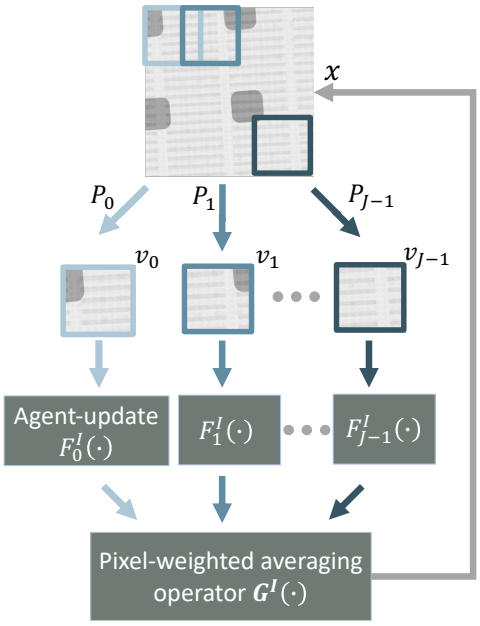

Figure 2: Conceptual overview of the PMACE pipeline for patch refinement. The state x is divided into overlapping components v_j, and distributed to multiple agents $F_j^I(\cdot)$ for local enhancement. These local reconstructions are then combined using a pixel-weighted averaging operator $\mathbf{G}^I(\cdot)$ to create an integrated global reconstruction, which ensures consistency within overlapping regions.

Then the PMACE equilibrium for the stacked patches is the solution, $\mathbf{v}^*$, to the equations

$$\mathbf{F}^I(\mathbf{v}^*) = \mathbf{G}^I(\mathbf{v}^*) \ , \tag{4}$$

where $\mathbf{F}^I(\cdot)$ and $\mathbf{G}^I(\cdot)$ are operators introduced below and described in more detail in Section III-B.

The agent operator $\mathbf{F}^I(\cdot)$ is a stack of individual agents $F_j^I(\cdot)$ expressed as

$$\mathbf{F}^I(\mathbf{v}) = \left[F_0^I(v_0), \ldots, F_{J-1}^I(v_{J-1})\right]^t \ . \tag{5}$$

The agent $F_j^I(\cdot)$ refines the patch estimate $v_j = P_j x$ to make it more consistent with the measured data for the jth probe location. Notice that $F^I(\cdot)$ depends on the probe modes, d_k; however, we suppress this dependency for notational simplicity.

The consensus operator $\mathbf{G}^I(\mathbf{v})$ updates each patch using a weighted average that accounts for the current probe estimates and the patch overlaps in the image. Importantly, the consensus operator has the property that $\mathbf{G}^I(\mathbf{G}^I(\mathbf{v})) = \mathbf{G}^I(\mathbf{v})$ for all $\mathbf{v}$. Intuitively, this property means that averaging twice yields the same result as averaging once.

To solve the PMACE equations (4), we reformulate it as a fixed point problem. It is shown in [40] that Mann iterations can be applied to iteratively update $\mathbf{v}$ and converge to a fixed point of $\mathbf{T}^I = (2\mathbf{G}^I - \mathbf{I})(2\mathbf{F}^I - \mathbf{I})$ using

$$\mathbf{v} \leftarrow (1-\rho)\mathbf{v} + \rho \mathbf{T}^I \mathbf{v} \ , \tag{6}$$

where $\mathbf{I}$ denotes the identity operator, and $\rho \in (0,1)$ denotes the Mann averaging parameter. The choice of ρ controls the step size toward the fixed point. When $\mathbf{T}^I$ is non-expansive, this iterative calculation guarantees convergence to a solution of the PMACE equation if it has at least one fixed point solution.

B. Image Patch Update Agent

In this section, we define the agents in $\mathbf{F}^I(\cdot)$ and $\mathbf{G}^I(\cdot)$ of Eq. (4). To derive an expression for $F_j^I(v_j)$, we first observe that if y_j is the measured data, and v_j is a reasonably accurate estimate of the current patch, then Eq. (2) together with an assumption that the Poisson measurement is close to its mean implies that $y_j \approx \sqrt{\sum_{m=0}^{K-1} |\mathcal{F} D_m v_j|^2}$. Hence, for the kth mode, we can incorporate the y_j into a new, probe-dependent estimate of the patch by replacing the equality $v_j = D_{k,\epsilon}^{-1} \mathcal{F}^* (\mathcal{F} D_k v_j)$ with the update

$$\begin{aligned} \tilde{v}_{j,k} &= D_{k,\epsilon}^{-1} \mathcal{F}^* \left(\frac{y_j}{\sqrt{\sum_{m=0}^{K-1} |\mathcal{F} D_m v_j|^2}} \circ \mathcal{F} D_k v_j \right) \\ &= D_{k,\epsilon}^{-1} \mathcal{F}^* \left(y_j \circ \frac{\mathcal{F} D_k v_j}{\sqrt{\sum_{m=0}^{K-1} |\mathcal{F} D_m v_j|^2}} \right) \ , \end{aligned} \tag{7}$$

where $\circ$ denotes point-wise multiplication, $\mathcal{F}^*$ denotes the inverse (i.e., adjoint) Fourier transform, and $D_{k,\epsilon}^{-1}$ denotes a numerically stable inversion of D_k.[2]

Using Eq. (7), we define the agent F_j as a weighted sum

$$F_j^I(v_j) = (1-\alpha_1) v_j + \alpha_1 \sum_{k=0}^{K-1} w_k \circ \tilde{v}_{j,k} \ , \tag{8}$$

where

$$w_k = \frac{\|D_k\|_2^2}{\sum_{m=0}^{K-1} \|D_m\|_2^2} \ . \tag{9}$$

Note that w_k is a scalar that weights the estimates in proportion to their power, and α_1 is a parameter that controls the weighting between the previous and new patch estimates. We stack the data-fitting agents in Eq. (8) to create the data-fitting operator that updates the complex transmittance patches.

The consensus operator $\mathbf{G}^I(\mathbf{v}) = [P_0 \bar{v}, \ldots, P_{J-1} \bar{v}]^t$ is computed by using P_j^T to position each patch in context in the full image, and forming a weighted average using the probe pixel-wise intensities and the probe power weights as in Eq. (9). This gives

$$\bar{v} = \sum_{k=0}^{K-1} w_k \Lambda_k^{-1} \sum_{j=0}^{J-1} P_j^T |D_k|^\kappa v_j \ , \tag{10}$$

where $\Lambda_k = \sum_{j=0}^{J-1} P_j^T |D_k|^\kappa P_j$, and $1 \le \kappa \le 2$ is a parameter that effectively controls the weighting as a function of the probe strength. It is easily shown that $\mathbf{G}^I$ has the required property that $\mathbf{G}^I(\mathbf{G}^I(\mathbf{v})) = \mathbf{G}^I(\mathbf{v})$. Intuitively, $\mathbf{G}^I$ results in a pixel-weighted and mode-weighted average of the patches. The solution $\mathbf{v}^*$ is then computed using iterative updates as shown in Eq. (6).

[2]We compute the numerically stable inverse of the diagonal entries as $d_\epsilon^{-1} = d^*/(|d|^2 + \epsilon)$ where $\epsilon = 10^{-6}\sqrt{\|d\|^2/\dim(d)}$.

IV. Probe Reconstruction using PMACE

A key feature of BM-PMACE is the use of separate probe estimates at each probe location and a consensus operator that produces a single probe estimate from these individual estimates. This approach makes efficient use of the complementary information inherent in patches with different transmission images while also producing a single estimate that informs each individual estimate.

Figure 3 illustrates the PMACE pipeline for probe refinement. An initial probe estimate is distributed to multiple agents, each associated with a specific scan position. Each agent makes adjustments to its probe estimate using the associated patch transmittance estimate and corresponding measurements. As in the pipeline in Figure 3, these local estimates are then averaged to update the global probe, ensuring consistency between different scan locations.

Intuitively, this algorithm maintains local and global probe mode estimates through $d_{j,k}$ and $\bar{d}_k$, respectively. The local estimate, based on the characteristics of the reconstructed image and data in a patch, allows the probe modes to adapt to specific variations encountered at each scan location. The global estimate, formed by the average of these local estimates, averages out local variations and is used to update the transmission image. In the results section, we show that by keeping this combination of local and global probe estimates, our algorithm achieves fast and robust convergence to a high-quality reconstruction.

A. Probe Update Pipeline

In this section, we outline the PMACE algorithm used to estimate the probe modes assuming a known transmission image, x. In Sec. IV-B, we describe the local probe update agent, and in Sec. V we combine probe and patch estimation.

For probe estimation, we define the collection of probe modes indexed by k, which is formed from the estimates at each of J probe locations to yield

$$\mathbf{d}_k = [d_{0,k}, \dots, d_{J-1,k}]^t \ . \tag{11}$$

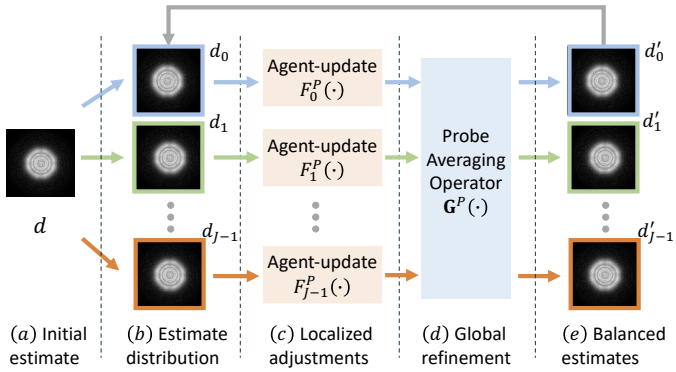

Figure 3: Illustration of the PMACE pipeline for multi-mode probe estimation, illustrated here for a single mode. The pipeline starts by distributing the global probe estimate d to multiple agents. Each probe agent then performs a localized adjustment using its own update function $F_j^P(\cdot)$. The locally refined probe estimates are then averaged by $\mathbf{G}^P(\cdot)$ to form an array of identical estimates.

For the estimate of the kth mode at the jth location, we define an associated agent $F_{j,k}^P$ (described in Sec. IV-B) that updates the corresponding probe estimate. This allows the local probe updates to be performed independently based on the associated measurements and patch transmittance. We stack these individual updates to form the operator

$$\mathbf{F}_k^P(\mathbf{d}_k) = \left[F_{0,k}^P(d_{0,k}), \dots, F_{J-1,k}^P(d_{J-1,k})\right]^t \ . \tag{12}$$

Each $F_{j,k}^P$ depends on the patch x_j, but we suppress this dependence for simplicity.

We define the consensus operator for the probes to be a simple average of the local probe mode estimates given by

$$\mathbf{G}^P(\mathbf{d}_k) = \left[\bar{d}_k, \dots, \bar{d}_k\right] \ , \tag{13}$$

where $\bar{d}_k = \frac{1}{J}\sum_{j=0}^{J-1} d_{j,k}$.

As before, we find the PMACE solution for each probe mode as the fixed point of the operator $\mathbf{T}_k^P = (2\mathbf{G}_k^P - \mathbf{I})(2\mathbf{F}_k^P - \mathbf{I})$ using Mann iterations

$$\mathbf{d}_k \leftarrow (1-\rho)\mathbf{d}_k + \rho\mathbf{T}_k^P\mathbf{d}_k \ . \tag{14}$$

B. Local Probe Update Agent

For the local probe update, we need to incorporate the existing probe estimate, d_j, with the patch measurements, y_j, and the patch transmittance estimate, $P_j x$. We multiply the probe mode by the transmittance, take the Fourier transform, multiply by the measured values normalized by the full probe amplitude, then take the inverse Fourier transform and divide by the patch to get the new probe mode update. This gives

$$\tilde{d}_{j,k} = X_{j,\epsilon}^{-1}\mathcal{F}^*\left(y_j \circ \frac{\mathcal{F}X_j d_{j,k}}{\sqrt{\sum_{m=0}^{K-1}|\mathcal{F}X_j d_{j,m}|^2}}\right) \ , \tag{15}$$

where $X_j = \mathrm{diag}(P_j x)$ is a diagonal matrix representing the patch transmittance and $X_{j,\epsilon}^{-1}$ denotes the stable inverse of X_j with ϵ added for numerical stability. The full update for $d_{j,k}$ is then

$$F_{j,k}^P(d_{j,k}) = (1-\alpha_2)d_{j,k} + \alpha_2\tilde{d}_{j,k} \ , \tag{16}$$

where α_2 controls the balance between the current estimate of the mode and the new estimate.

Note that our probe update agent uses all probe modes $\tilde{d}\,(d_{j,*})$, along with the current image patches, $v_j = P_j x$, in its update. However, each agent refines one specific mode at a time. For clarity, we suppress this dependency in Eq. (16). The probe data-fitting agent makes localized adjustments that are specific to the characteristics of the data collected at that position.

V. Integrated PMACE Algorithm for Blind Multi-mode Reconstruction

In this section, we integrate the PMACE algorithms for reconstruction of the transmission image, x and the probe modes, d_k, for $k = 0, \dots K-1$. We first present the pseudo-code for implementation, followed by an explanation of the initialization process and the adaptive mode addition strategy.

Algorithm 1 BM-PMACE algorithm.

Input: Initialization: $x^{(0)} \in \mathbb{C}^{N_1 \times N_2}$, $d^{(0)} \in \mathbb{C}^{N_p \times N_p}$, $K = 1$
Design parameters: $\kappa = 1.25$, $\rho = 0.5$
Output: Final Reconstruction: $\hat{x} \in \mathbb{C}^{N_1 \times N_2}$; $\hat{d}_k \in \mathbb{C}^{N_p \times N_p}$

```
w = z = v = [v_0^(0), ..., v_{J-1}^(0)], where v_j^(0) = P_j x^(0)
r_0 = s_0 = u_0 = [d_0^(0), ..., d_{J-1}^(0)],
while not converged do
    // Update the image patches
    w ← F^I(v; u_*)
    z ← G^I(2w − v; u_*)
    v ← v + 2ρ(z − w)
    // Update K probe modes
    for k = 0 to K − 1 do
        r_k ← F_k^P(s_k; s_*, z)
        u_k ← G^P(2r_k − s_k)
        s_k ← s_k + 2ρ(u_k − r_k)
    end for
    // Adaptive mode addition
    if more modes needed then
        Add mode using Eq. (19)
        K ← K + 1
    end if
end while
return x̂ ← Σ_{k=0}^{K−1} w_k Λ_k^{−1} Σ_{j=0}^{J−1} P_j^T |D_k|^κ v_j;
       d̂_* ← Σ_{j=0}^{J−1} s_{j,*}
```

Algorithm 1 provides the pseudo-code for computing the BM-PMACE solution. The algorithm starts with an initial estimate of the complex transmittance image $x^{(0)}$ and an initial estimate of a single complex probe function $d^{(0)}$. The number of probe modes, K, is initialized to 1. We set $\rho = 0.5$ as the default value for the Mann averaging parameter, which provides a practical balance between convergence speed and stability. The probe weight parameter is set as $\kappa = 1.25$ since we find that it provides fast convergence speed and high reconstruction quality.

The initial vectors $\mathbf{w}$ and $\mathbf{v}$ are created from the projections of $x^{(0)}$, and the vectors $\mathbf{r}_0, \mathbf{s}_0$ and $\mathbf{u}_0$ are created from $d^{(0)}$. Within each iteration, the algorithm performs updates to the complex transmittance image and probe function alternatively and the main loop continues until convergence is achieved. Note that $\mathbf{F}^I(\cdot)$ and $\mathbf{F}_k^P(\cdot)$ both depend on all current probe modes denoted by $\mathbf{u}_*$. This implies that image patches are updated using all current probe modes, and each probe mode is then updated using the new patch estimates and the other probe modes, and $\mathbf{F}_k^P(\cdot)$ also depends on the current transmission estimate denoted by $\mathbf{z}$. Additional modes are added if necessary for better reconstruction quality. The final reconstruction is obtained by computing $\hat{x}$ from the weighted average of the complex transmittance patches, v_j.

The computational complexity of BM-PMACE is dominated by FFTs performed during image and probe updates. For each iteration, each patch and probe mode require forward and inverse FFTs at every probe location. The per-iteration complexity is $\mathcal{O}(J \cdot K \cdot N_p^2 \log N_p)$. The memory needed for distributed probe storage is $\mathcal{O}(J \cdot K \cdot N_p^2)$. And the object patches at each scan location requires additional storage of $\mathcal{O}(J \cdot N_p^2)$. As each agent's update can be computed independently, BM-PMACE is well-suited for distributed computing environments.

Notice that the BM-PMACE algorithm interlaces updates associated with the image patch agent, $\mathbf{F}^I$, and each probe mode agent, $\mathbf{F}_k^P$. These updates are performed in sequence, which aids in fast convergence, but each agent allows parallel updates at each location of the probe. We note that standard proofs of mathematical convergence no longer apply with interlaced updates. However, in practice, we have empirically observed that the algorithm converges robustly as demonstrated in Section VI.

A. Initialization Method

Initialization is a critical step in ptychographic reconstruction that can significantly impact the reconstruction speed, quality, and robustness, particularly when dealing with large datasets or noisy datasets.

We start by setting the initial probe mode to

$$d^{(0)} \leftarrow U_{\eta,z,\triangle_x} \left\{ \frac{1}{J} \sum_{j=0}^{J-1} \left(P_j \mathbf{1}\right)^{-1} \mathcal{F}^* y_j \right\} , \qquad (17)$$

where $\mathbf{1}$ is a vector of ones, $U_{\eta,z,\triangle_x}$ denotes Fresnel propagation as a function of source wavelength η, propagation distance z and sampling rate $\triangle_x$. Our practical experience has shown that introducing some phase information through the Fresnel propagator facilitates efficient reconstruction and fast convergence to favorable results. Next, we initialize the transmittance image using the formula:

$$x^{(0)} \leftarrow \Lambda_0^{-1} \sum_{j=0}^{J-1} P_j^T \left(\frac{\|y_j\|}{\|d^{(0)}\|} \mathbf{1} \right) , \qquad (18)$$

where $\Lambda_0 = \sum_{j=0}^{J-1} P_j^T P_j$ and $\mathbb{1}$ is a column vector of 1s. This approach ensures the initialized images match the strength of the data collected at different scan locations.

B. Adding Probe Modes

To perform reconstruction with multiple modes, we first run reconstruction algorithms with initialized images for an adequate number of iterations. Subsequent to these iterations, we incorporate the additional modes as needed. We then add additional probe modes through the following calculation

$$d_K \leftarrow U_{\eta,z,\triangle_x} \left\{ \frac{1}{J} \sum_{j=0}^{J-1} X_j^{-1} \left[\mathcal{F}^* \sqrt{\max\left(0, I_{\text{res}}\right)} \right] \right\} , \qquad (19)$$

where $I_{\text{res}} = I_j - \sum_{k=0}^{K-1} |\mathcal{F} D_k x_j|^2$ calculates the residual intensity, the $\max(\cdot)$ function ensures the argument of the square root function is non-negative.

After that, we scale the power of all the probes to ensure that the total power matches the original total power prior to the incorporation of the new mode. This step is critical to maintaining a consistent power distribution across the probes and preventing a single mode from dominating the reconstruction process.

VI. Experimental Results

In this section, we present the results of experiments using both synthetic and measured data[3].. We introduce our data simulation process and show experiment results using both single and multiple probe modes for different light sources. Our findings demonstrate that BM-PMACE improves the quality of reconstructions and the robustness of convergence across a range of imaging scenarios.

In all experiments, with both synthetic and measured data, we used $\rho = 0.5$, $\kappa = 1.25$, and $\alpha_2 = 0.6$. For the single-mode cases, we used $\alpha_1 = 0.6$, and in the two-mode cases, we used $\alpha_1 = 0.5$.

A. Single-Mode Blind Reconstruction: Synthetic Data

1) Single-Mode Data Simulation: The ground truth image is complex-valued and consists of an 800×800 array of pixels that models the transmission characteristics of a 5-layer composite material. The ground truth probe used for sampling the object image was simulated with a photon energy of 8.8 keV and has dimensions of 256×256 pixels. We show the plot of the ground truth images and probes in Figure 4.

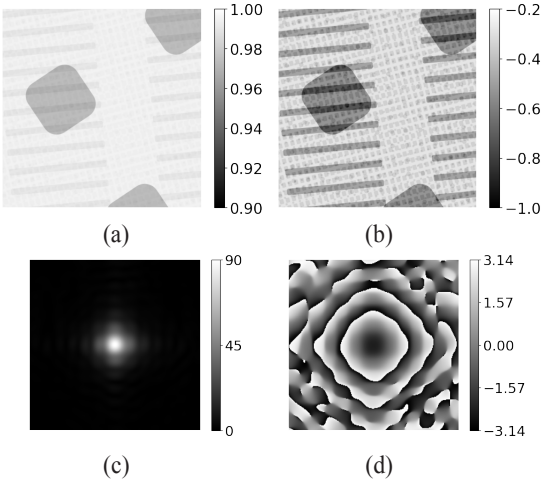

Figure 4: Simulated single-mode ground truth image (top) and probe function (bottom): (a) Magnitude and (b) phase in radians of the complex ground truth object; (c) Magnitude and (d) phase in radians of the probe function. This image and probe are used for results in Figures 5–10.

We used the following formula to simulate the measurements for the j^{th} probe location

$$\hat{y}_j \leftarrow \sqrt{\text{Pois}\left(r_p \frac{I_j}{\max_i(\|I_i\|_\infty)} + \lambda\right)}\ , \tag{20}$$

where $I_j = \sum_{k=0}^{K-1} |\mathcal{F} D_k P_j x|^2$, $\|\cdot\|_\infty$ denotes the infinity norm, and $\max_i(\cdot)$ denotes the maximum value over all i. For our simulation of coherent data, we assumed a photon detector with 14-bit dynamic range and the presence of a half-bit of dark current, using $K = 1$, $r_p = 10^4$ and $\lambda = 0.5$.

We generate random probe locations on a rectangular grid separated by a nominal distance of 36 pixels, but with random offsets uniformly chosen within the range [-5, 5] pixels for each point. This approach resembles practical ptychographic experiments and helps avoid periodic reconstruction artifacts [42]. This resulted in a probe overlap ratio of $r_{ovlp} \approx 44\%$ using the definition of probe overlap ratio defined in [40].

2) Single-Mode Reconstruction Results: Blind reconstructions were performed using the ePIE, AWF, SHARP, and BM-PMACE approaches. We optimized the algorithmic parameters for each method using grid search and ran each method for 100 iterations. To quantitatively assess the reconstruction quality, we use the normalized root mean square error (NRMSE) value between the complex-valued reconstructed image $\hat{x}$ and the ground truth image x using

$$NRMSE = \min_{c \in \mathbb{C} \setminus \{0\}} \frac{\|c\hat{x} - x\|}{\|x\|}\ , \tag{21}$$

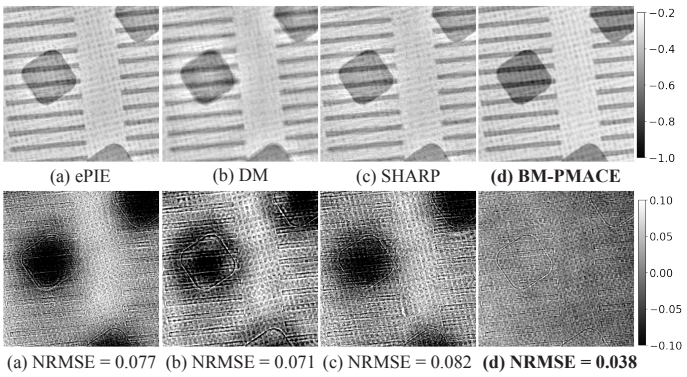

Figure 5: Single-mode reconstructions of complex-valued object from data in Figure 4 using multiple algorithms. Top: **Phase** (in radians) of the reconstructed complex transmittance images from synthetic single-mode data. Bottom: Difference between the reconstructed and ground truth phase, with NRMSE for the complex-valued reconstructions indicated in the subcaptions. BM-PMACE achieves the lowest NRMSE among these methods.

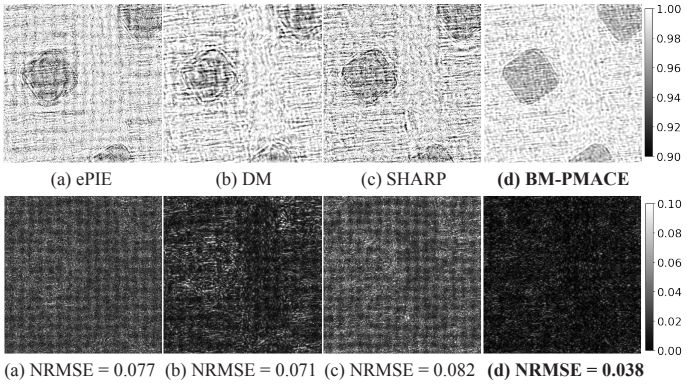

Figure 6: Single-mode reconstructions of complex-valued object from data in Figure 4 using multiple algorithms. Top: **Magnitude** of the reconstructed complex transmittance images from synthetic single-mode data. Bottom: Amplitudes of error between the complex reconstructions and ground truth. BM-PMACE visually outperforms the other methods.

[3]The code for reproducing experimental results is available at https://github.com/cabouman/ptycho_pmace_papers.

where c accounts for possible nonunit gain and an unknown phase shift (since ptychographic measurements are invariant to a constant phase shift in the image domain).

Figures 5 and 6 show the reconstructed phases and magnitudes for the transmittance image obtained using ePIE, DM, SHARP, and BM-PMACE. The NRMSE values are included in the bottom caption of each image; these are NRMSE for the complex volume and so are the same in Figures 5 and 6. In each case, BM-PMACE produced substantially lower reconstruction error than the alternative methods.

Figures 7 and 8 show the reconstructions and reconstruction error for both the phase and magnitude of the probe resulting from ePIE, DM, SHARP, and BM-PMACE. The reconstructed phase using ePIE exhibits significant noise, while DM reconstruction mainly shows noise in the border region. The SHARP probe contains artifacts near the edges. Again, the BM-PMACE reconstructions have substantially lower reconstruction error than the alternative methods.

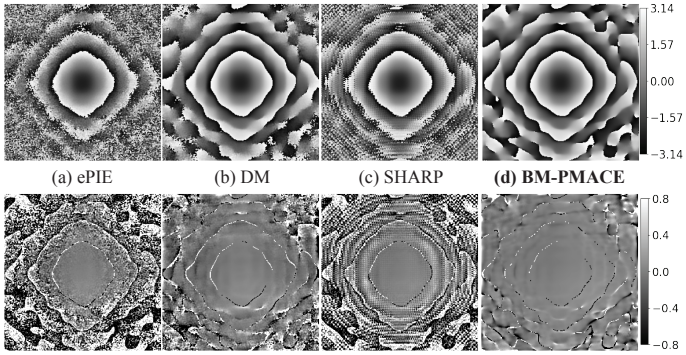

Figure 7: Single-mode reconstructions of complex-valued probe from data in Figure 4 using multiple algorithms. Top: **Phase** (in radians) of the reconstructed probes from synthetic single-mode data. Bottom: Difference between the reconstructed and ground truth phase, with NRMSE for the complex-valued probe indicated in the subcaptions. BM-PMACE achieves the most accurate reconstruction.

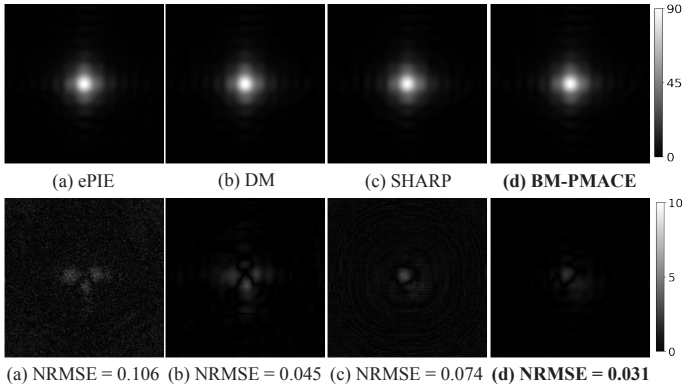

Figure 8: Single-mode reconstructions of complex-valued probe from data in Figure 4 using multiple algorithms. Top: **Magnitude** of the reconstructed probes from synthetic single-mode data. Bottom: Amplitudes of error between the complex reconstructions and ground truth. BM-PMACE shows reduced error artifacts in the bottom-right.

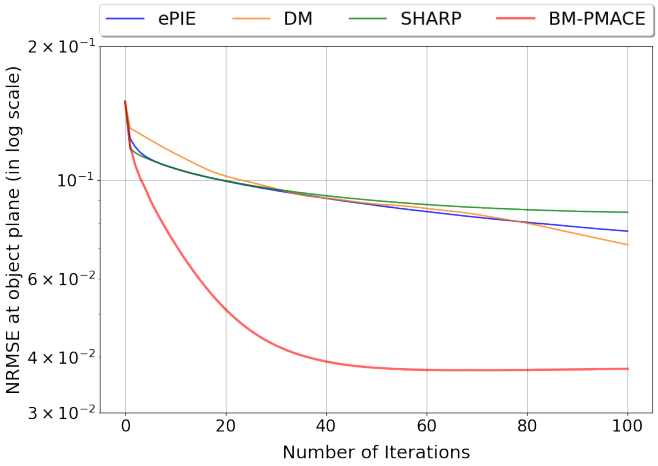

Figure 9: Reconstruction accuracy of complex-valued object from synthetic single-mode data in Figure 4. Plotted is the NRMSE between reconstructed object images and ground truth as a function of the number of iterations on synthetic single-mode data with probe overlap ratio 44%. The lower NRMSE indicates better reconstruction performance.

Figure 9 presents the convergence of the NRMSE as a function of the number of iterations for ePIE, DM, SHARP, and BM-PMACE. BM-PMACE demonstrates a significantly faster convergence rate and reaches stable solutions within about 50 iterations. This indicates the efficiency of BM-PMACE and also its robustness to the presence of noise.

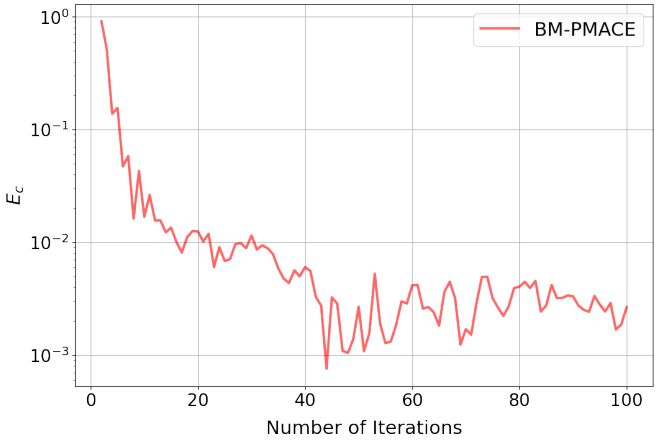

Figure 10: Convergence of patch updates in BM-PMACE tracked by the error metric E_c as a function of iterations. E_c decreases rapidly at the beginning and stabilizes at a low value of 10^{-3}, indicating consistent refinement over iterations.

Figure 10 illustrates the convergence of BM-PMACE as a function of the number of iterations. Here, convergence is measured by the quantity $E_c = \frac{1}{J}\left\|\mathbf{z} - \mathbf{w}\right\|_2$, where $\mathbf{w}$ and $\mathbf{z}$ are variables introduced in Algorithm 1 and J is the number of patches. Notice that as E_c approaches zero, the output of $\mathbf{F}^I(\cdot)$ and $\mathbf{G}^I(\cdot)$ become equal, and the desired equilibrium condition of Eq. (4) holds. Consequently, the plot of Figure 10

indicates that the BM-PMACE algorithm converges to an equilibrium, up to some inherent uncertainty.

B. Multi-Mode Blind Reconstruction: Synthetic Data

1) Multi-Mode Data Simulation: Figure 11 shows the $K = 2$ probe modes used for the simulation along with the 256×256 pixel ground truth image. As with the single-mode experiment, this ground truth image is based on a simulated transmission measurement through a composite material. The probe modes are 256×256 pixels and were used in Eq. (20) with $K = 2$ to generate the simulated data. As in the single-mode experiment, probe locations were generated on a rectangular grid with randomized offset and an average probe spacing of 36 pixels. The probe modes were constructed so that the main probe mode occupied 90% of the total energy, resulting in an overlap ratio of the main probe mode of $r_{\mathrm{ovlp}} \approx 65\%$.

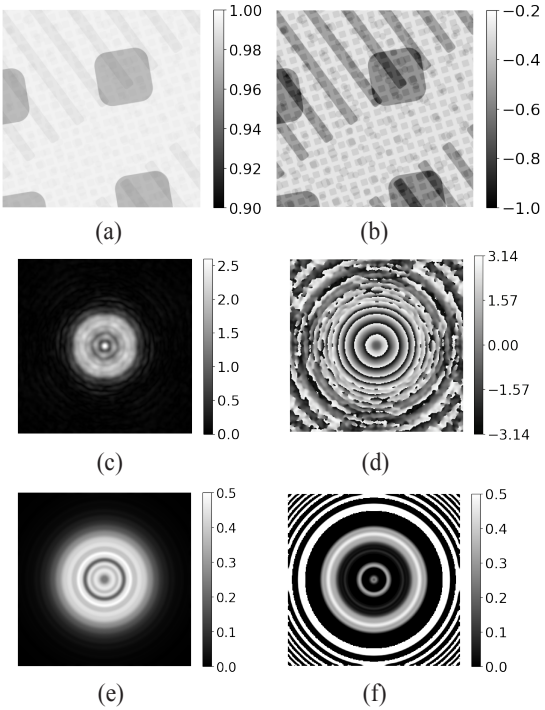

Figure 11: Simulated multi-mode ground truth image and mutually incoherent probe modes. The complex ground truth object's (a) magnitude and (b) phase; The main probe mode function's (c) magnitude and (d) phase; The secondary probe mode function's (e) magnitude and (f) phase. These images are used for results in Figures 12–15.

2) Multi-Mode Reconstruction Results: We performed reconstruction using ePIE, DM, and BM-PMACE, each for 200 iterations. For all methods, the initializations followed our approach, and the secondary probe mode was initialized and introduced to the reconstruction process after 20 iterations.

Figures 12 and 13 show the reconstructed phases and magnitudes obtained using the ePIE, DM, and BM-PMACE methods. Also, the left column in both figures shows the reconstructed images using BM-PMACE with single-mode, which does not fully capture the details in ground truth image. Note that the transmittance phase is typically more important than magnitude in many applications. This is because phase information often provides much higher contrast than magnitude information. In addition, the phase shift is directly related to the optical path length through the object, which provides quantitative information about the sample's thickness and refractive index. Our results indicate that BM-PMACE method produces images with significantly fewer artifacts compared to the other approaches and substantially lower NRMSE.

Figure 14 shows the reconstructed probe images, including the reconstructed magnitudes and phases of both the main probe mode and the secondary probe mode. These figures illustrate the detailed structure of the reconstructed probe modes for each method. BM-PMACE consistently captures the complex features of the illumination with greater precision, while ePIE and DM exhibit more distortions and less accurate probe mode representations.

Figure 15 shows convergence plots for synthetic multi-mode data. ePIE exhibits fast initial convergence but fails to reach an optimal solution. DM converges to a better solution than ePIE but requires significantly more iterations. DM continues to improve after 200 iterations, which can result in excessively

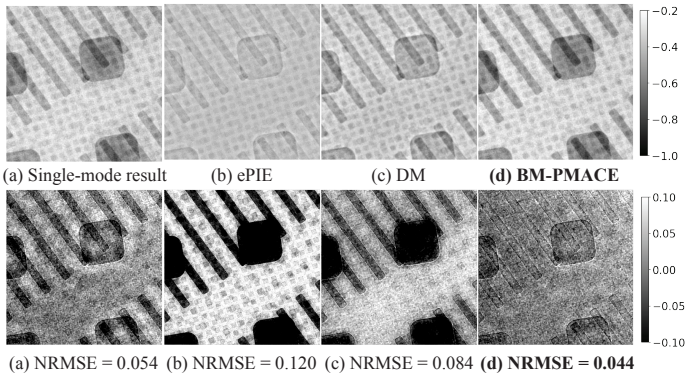

Figure 12: Multi-mode reconstructions of complex-valued object from data in Figure 11 using multiple algorithms. Top: **Phase** (in radians) of the reconstructed complex transmittance images. Bottom: Difference between the reconstructed and ground truth phase. BM-PMACE achieves the lowest NRMSE among the tested methods.

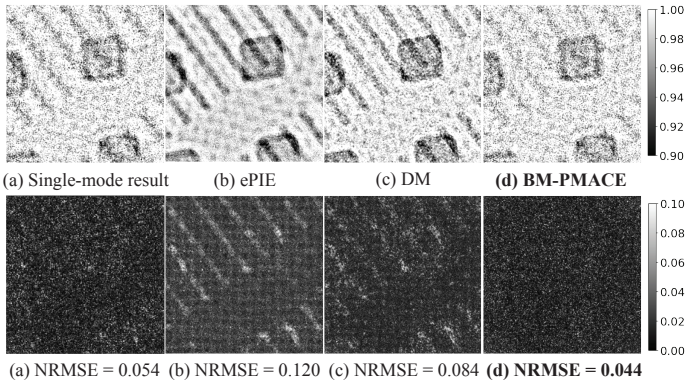

Figure 13: Multi-mode reconstructions of complex-valued object from data in Figure 11 using multiple algorithms. Top: **Magnitude** of the reconstructed complex transmittance images. Bottom: Amplitdues of error between the complex reconstructions and ground truth. BM-PMACE exhibits the least residual error in the difference image.

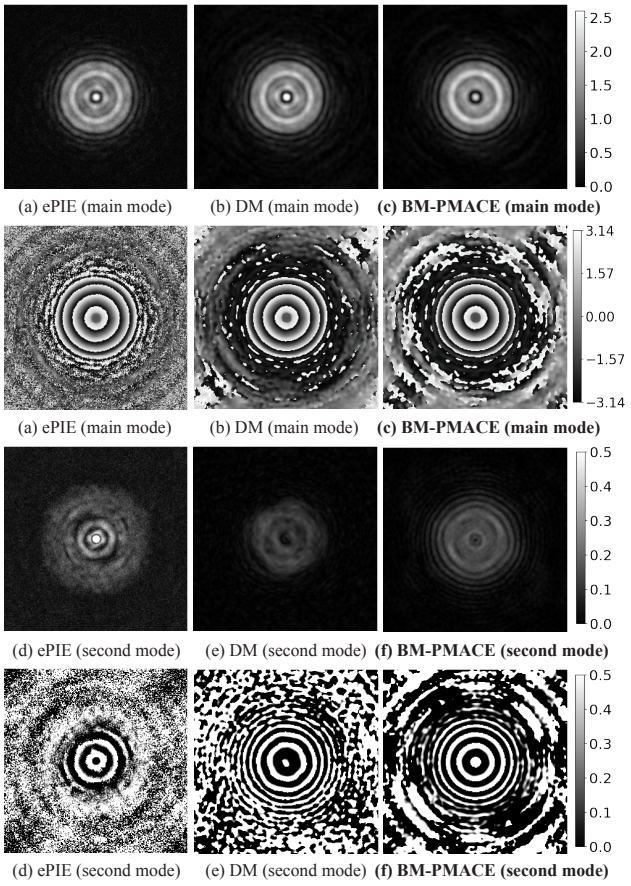

Figure 14: Multi-mode reconstructions of complex-valued probes from data in Figure 11 using multiple algorithms. Top row: Magnitudes of the reconstructed complex probe functions for the main mode, using ePIE, DM, and BM-PMACE. Second row: Phase (in radians) of the reconstructed complex probe function for the main mode. Third and fourth rows: Magnitudes and phases (in radians) of the reconstructed complex probe function for the secondary mode from multi-mode data. BM-PMACE reconstructs both the main and secondary probe modes with greater clarity and fewer artifacts.

long computational time. BM-PMACE has substantially faster convergence as compared to ePIE and DM and the solution it reaches has much lower NRMSE than ePIE and DM.

C. Scan Position Refinement

The ptychographic reconstruction algorithms critically depend on accurate scan position information. The scan position errors due to mechanical drift or calibration inaccuracies can significantly degrade reconstruction quality. In this section, we present the scan position refinement algorithm integrated with the BM-PMACE framework. Our approach iteratively optimizes scan positions using a grid-based search and parallel computation.

For each scan position, a grid search is performed in a local $N_s \times N_s$ pixel neighborhood (e.g. 5 x 5) to find the offset that minimizes intensity error. We evaluate the quality of candidate scan positions by comparing simulated intensity from the current object and probe estimate with measured intensity data

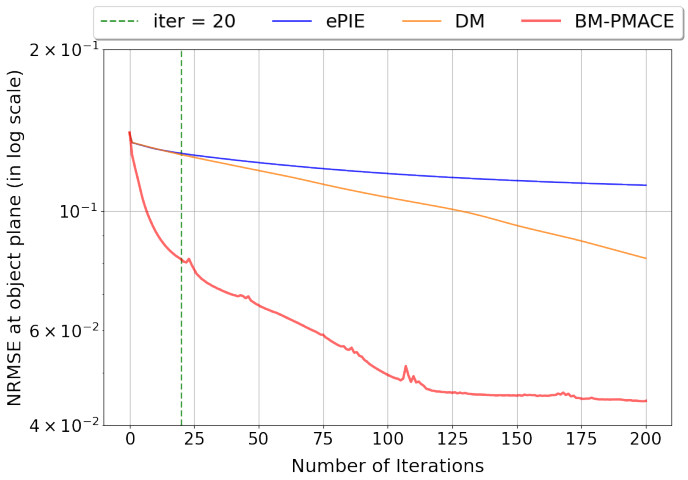

Figure 15: Reconstruction accuracy of complex-valued object from synthetic multi-mode data in Figure 11. Plotted is the NRMSE between reconstructed object images and ground truth as a function of number of iterations on synthetic multi-mode data. BM-PMACE achieves faster convergence and higher accuracy in reconstructing the object.

using the Frobenius norm as the error metric. After identifying the optimal offset, we update the scan position and continue BM-PMACE reconstruction with refined positions.

Large scan position errors may require multiple refinement iterations. Our scan position refinement algorithm allows users to specify exactly at which reconstruction iterations scan position refinement should be performed. In the following experiments, we first run the main BM-PMACE reconstruction for 10 iterations to allow the object and probe to achieve initial improvement and then trigger scan position refinement at user-defined iterations. After refinement steps, the finalized scan positions are recorded and consistently used for all reconstruction approaches for comparative analysis.

1) Single-mode Blind Reconstruction with Scan Position Refinement: To simulate experimental uncertainties, scan positions are perturbed by adding Gaussian noise with a standard deviation of 2 pixels, which is about 5.6% of the average 36-pixel distance between neighboring scan points.

The experiment proceeded in two stages. First, we performed PMACE recosntruction for 10 iterations, then enabled scan position refinement for 3 iterations, allowing the algorithm to correct scan position errors using a 3x3 grid search with a one-pixel step size. The refined scan positions were saved and used for the following reconstructions. Next, we conducted reconstruction using the corrected positions.

Figures 16 and 17 show the reconstructed phase and magnitude images for the synthetic noisy data using single-mode approaches with corrected scan positions. BM-PMACE achieves the lowest NRMSE and provides the most accurate results among the tested algorithms.

Figure 18 presents convergence comparison for tested algorithms. The impact of scan position errors is visualized by the dashed blue line. The position errors degrade the performance of BM-PMACE, both in terms of convergence speed and final accuracy. The algorithms shown with solid lines, including ePIE, DM, SHARP, and BM-PMACE, are evaluated and tested

with corrected scan positions. The plot demonstrates that the position-corrected BM-PMACE consistently outperforms the other methods.

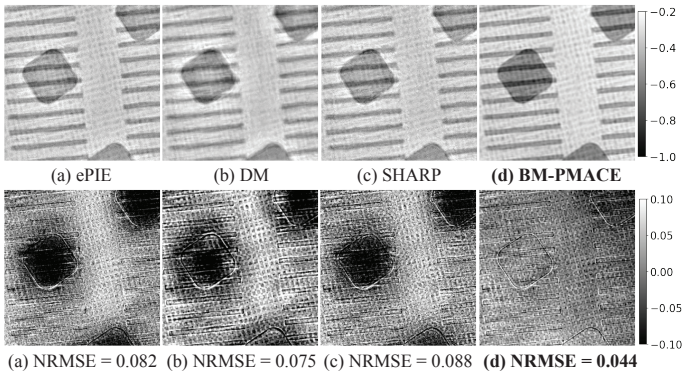

Figure 16: **Position-corrected** single-mode reconstructions of complex-valued object from data in Figure 4. Top: **Phase** (in radians) of the reconstructed images. Bottom: Difference between reconstructed and ground truth phase.

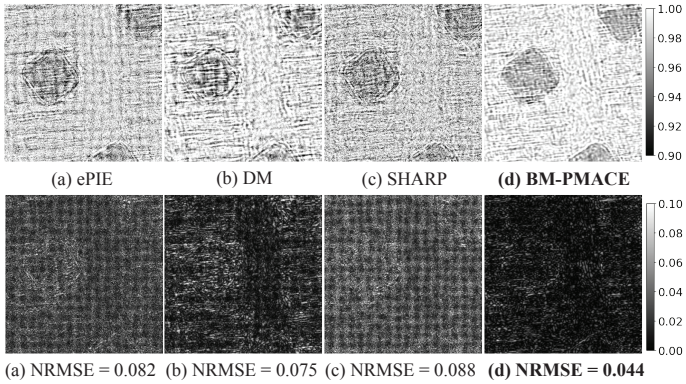

Figure 17: **Position-corrected** single-mode reconstructions of complex-valued object from data in Figure 4. Top: **Magnitude** of the reconstructed complex transmittance images. Bottom: Amplitudes of error between reconstructions and ground truth.

2) Two-mode Blind Reconstruction with Scan Position Refinement: Building on the single-mode setup, we simulate experimental uncertainties to the multi-mode experiment as before. The scan positions are perturbed by adding Gaussian noise with a standard deviation of 2 pixels.

We first corrected the perturbed scan positions by running BM-PMACE for 10 iterations to jointly update the object and single probe mode. This was followed by 3 iterations of scan position refinement, using a 3x3 grid search with one-pixel step size. The refined scan positions were saved and used for the final reconstructions. All reconstruction methods shared the same corrected scan positions, initialization as described in Section V-A, and adaptive mode incorporation strategy outlined in Section V-B.

Figures 19 and 20 presents the results of position-corrected multi-mode reconstructions of the complex-valued transmittance image using ePIE, DM, and BM-PMACE, with the first column in both figures illustrating the reconstruction results using perturbed scan positions. The results from perturbed scan locations exhibit degraded image quality with artifacts and loss of details in both phase and magnitude reconstructions. Following scan position refinement, the reconstructions produced by BM-PMACE exhibit the clearest structural details and the smallest error maps among the reconstruction methods.

Figure 21 compares the convergence of multi-mode algorithms. The blue dashed line represents BM-PMACE with perturbed scan locations. Compared to the position-corrected BM-PMACE in red solid line, the perturbed version shows significantly higher NRMSE throughout the iterations. After scan position refinement, the NRMSEs at the object plane as a function of the number of iterations are shown in solid lines. BM-PMACE consistently achieves faster convergence and lowest final NRMSE.

D. Experimental Methods on Measured Data

In this section, we use the Ptychography Gold Ball Example Dataset that was collected by Marchesini using Lawrence Berkeley Laboratory's Advanced Light Source (ALS) [70]. The scans were performed on a 20×40 grid, with adjacent scans spaced 30 nm apart. A total of 800 ptychographic measurements were captured by the detector positioned 0.112 m downstream from the sample of nanometer-sized gold balls. Based on previous investigations with this dataset, the illumination overlap ratio is approximately 84%, which is sufficient to achieve high-quality reconstructions in ptychography [40].

In the preprocessing of the raw data, we subtracted the average of 20 dark scans from each intensity measurement. This step is critical for mitigating the influence of noise. Subsequently, a subset of 6 measurements exhibiting significant deviations are identified as outliers and excluded from the dataset. This step is crucial to mitigate the impact of inconsistencies in the data and to improve the fidelity of the reconstruction. For fast calculation of Fourier Transform, we

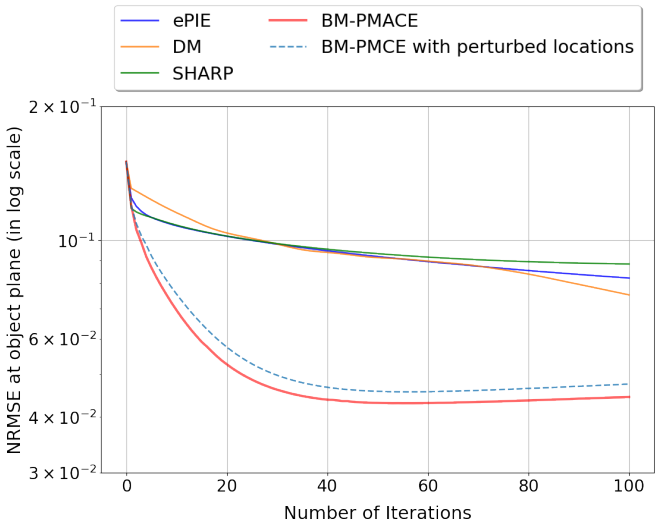

Figure 18: Convergence comparison of single-mode approaches using synthetic single-mode data in Figure 4. The plot contrasts BM-PMACE using perturbed scan locations (dashed blue) against approaches using corrected scan positions. Position-corrected BM-PMACE outperforms other approaches and achieves higher accuracy.

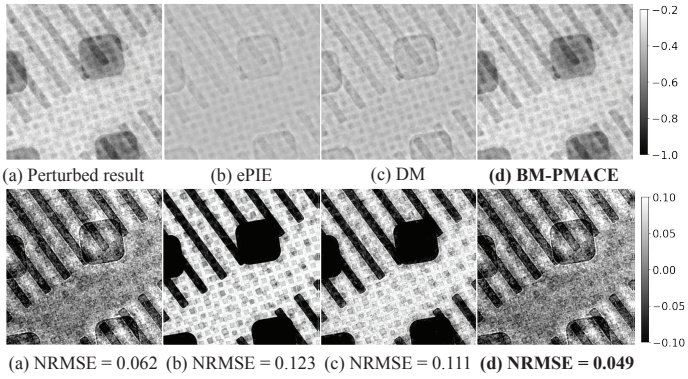

Figure 19: Position-corrected multi-mode reconstructions of complex-valued object from data in Figure 11 using multiple algorithms. Top: **Phase** (in radians) of the reconstructed complex transmittance images from synthetic multi-mode data. Bottom: Difference between the reconstructed and ground truth phase, with NRMSE values indicated in the subcaptions.

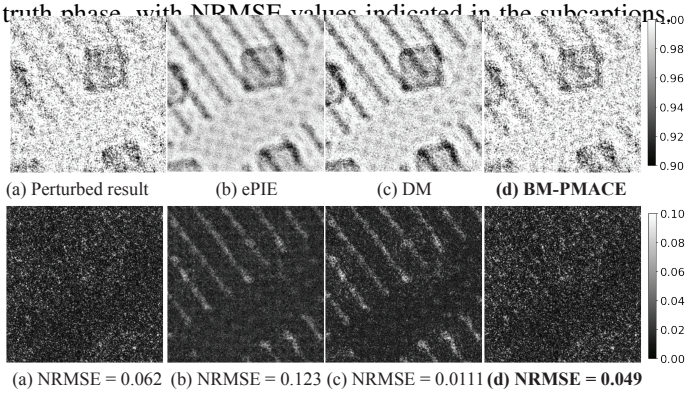

Figure 20: Position-corrected multi-mode reconstructions of complex-valued object from data in Figure 11 using multiple algorithms.Top: **Magnitude** of the reconstructed complex transmittance images from synthetic multi-mode data. Bottom: Amplitdues of error between the complex reconstructions and ground truth.

cropped each measurement and reduced the dimensions from 621×621 pixels to 512×512 pixels. While cropping diffraction pattern reduces the maximum scattering angle captured, this is an acceptable trade-off as the cropped data still contains sufficient high-frequency component for the reconstruction. To further enhance the data quality, we suppress noise by multiplying a 2D Tukey window to each of these diffraction measurements. The 2D Tukey window was generated by rotating a 1D Tukey window with shape parameter of 0.5. The resulting data set contains 794 preprocessed and high-quality diffraction measurements.

We refined the scan positions using BM-PMACE. This process involves 10 reconstruction iterations followed by 3 refinement iterations with 3x3 grid and one-pixel step size. Then we performed reconstructions using single-mode, $K = 1$, and two-mode, $K = 2$, approaches. For the single-mode reconstruction, we compared ePIE, DM, SHARP, and BM-PMACE; but for the two-mode reconstruction, we only compared ePIE, DM, and BM-PMACE, since SHARP does not support multi-mode reconstruction. To quantitatively compare

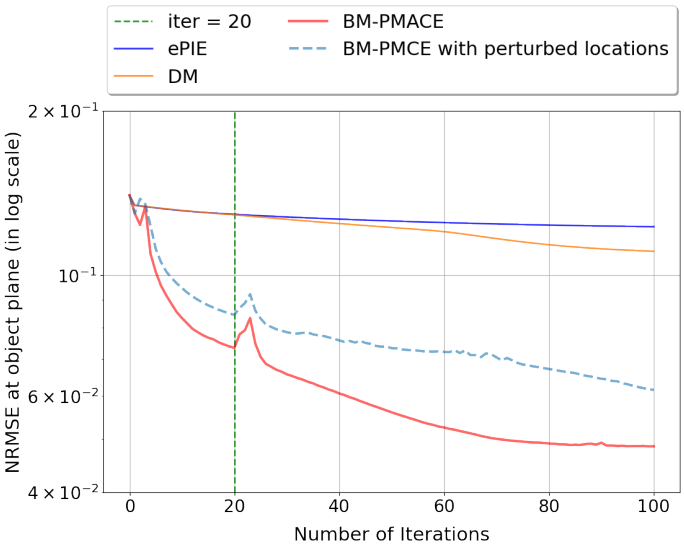

Figure 21: Convergence comparison of multi-mode approaches using synthetic multi-mode data in Figure 11. Plotted is the NRMSE between reconstructed object images and ground truth as a function of number of iterations on synthetic multi-mode data. Position-corrected BM-PMACE achieves faster convergence and lower NRMSE in reconstructing the object.

the different methods, we calculated the forward-propagated NRMSE metric in which we evaluated the NRMSE between the measured data and the estimated measurements obtained by passing the reconstruction and estimated probes through the forward model. Each method was run for a total of 100 iterations and parameters were selected to minimize the forward-propagated NRMSE. Initialization was performed as described in Section V-A.

E. Single-Mode and Multi-Mode Results: Measured Data

Figures 22 and 23 show the reconstructed phase and magnitude images for the Gold Ball dataset using single-mode and two-mode approaches. ePIE achieves good image quality in the central region, but has poor quality across the larger field-of-view. SHARP and DM are able to reconstruct features in a relatively larger field of view. However, they tend to reconstruct images with blurry details, especially near the edge of reconstructed images. BM-PMACE reconstructs the features across the largest field-of-view and exhibits significantly less noise compared to the other methods. In general, the two-mode reconstructions are superior to the one-mode reconstructions.

Figure 24 presents the probe estimates using ePIE, DM, SHARP, and BM-PMACE under the coherent probe assumption, where a single probe was reconstructed along with the object transmittance image. As the illumination overlap ratio is high and the data is sufficient for reconstruction, all methods produce high-quality probes with reliable and similar density distributions and wavefront shapes.

Figure 25 shows the reconstructed main mode and secondary mode using ePIE, DM, and BM-PMACE under the multiple probe modes condition, with the secondary probe introduced after 10 iterations. All reconstructed main probes

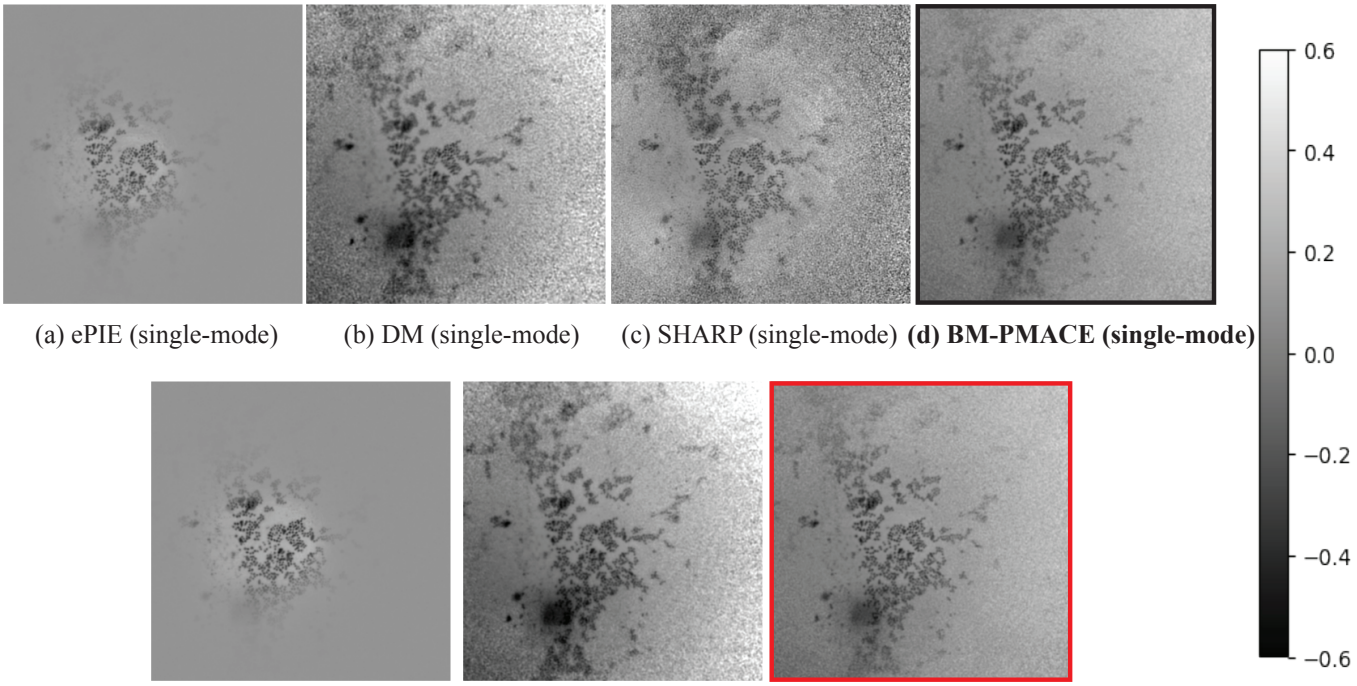

(a) ePIE (single-mode) (b) DM (single-mode) (c) SHARP (single-mode) **(d) BM-PMACE (single-mode)**

(e) ePIE (two-mode) (f) DM (two-mode) **(g) BM-PMACE (two-mode)**

Figure 22: **Phase** reconstructions (in radians) using single-mode and multi-mode algorithms from measured data.
The top row features the reconstructed images using ePIE, DM, SHARP, and BM-PMACE, using a single probe mode. The Bottom row shows the reconstructed images using ePIE, DM, and BM-PMACE, using two probe modes. BM-PMACE produces cleaner transmittance images than competing algorithms.

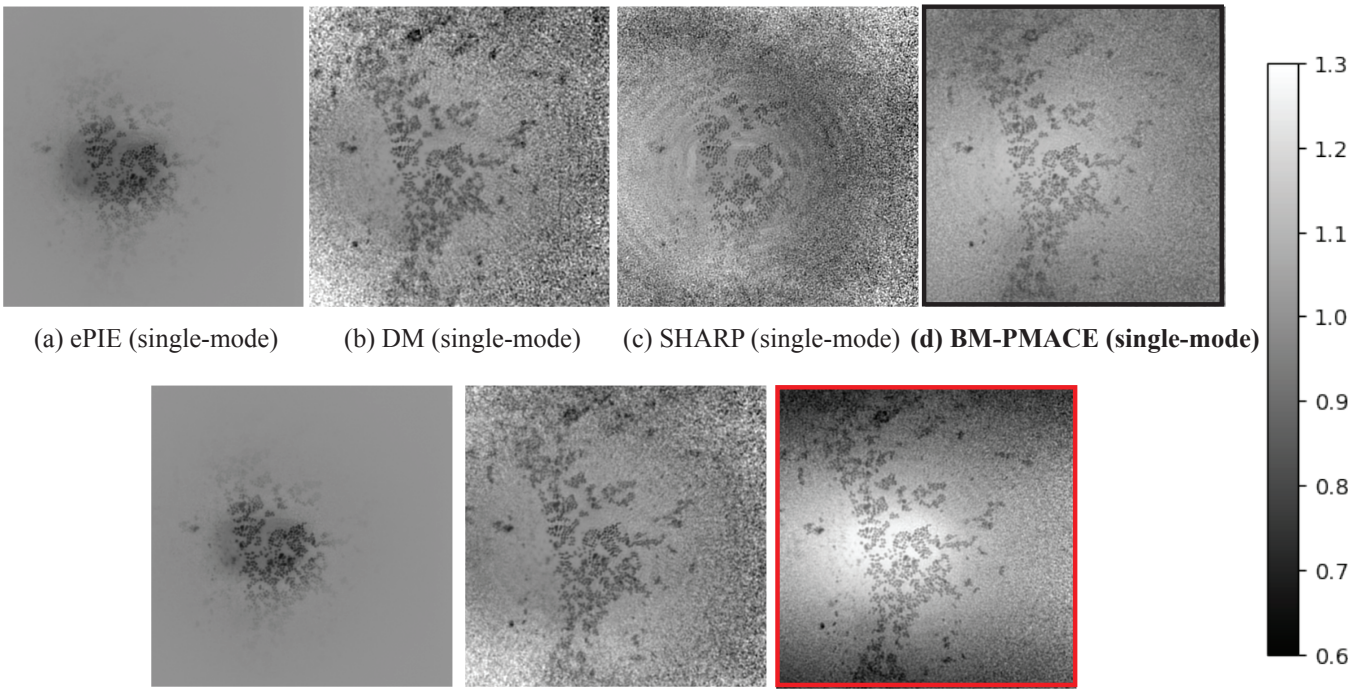

(a) ePIE (single-mode) (b) DM (single-mode) (c) SHARP (single-mode) **(d) BM-PMACE (single-mode)**

(e) ePIE (two-mode) (f) DM (two-mode) **(g) BM-PMACE (two-mode)**

Figure 23: **Magnitude** reconstructions of complex-valued object using single-mode and multi-mode algorithms from measured data.
The top row features the reconstructed images using ePIE, DM, SHARP, and BM-PMACE, using a single probe mode. The Bottom row shows the reconstructed images using ePIE, DM, and BM-PMACE, using two probe modes. Two-mode BM-PMACE results show better feature preservation and clarity.

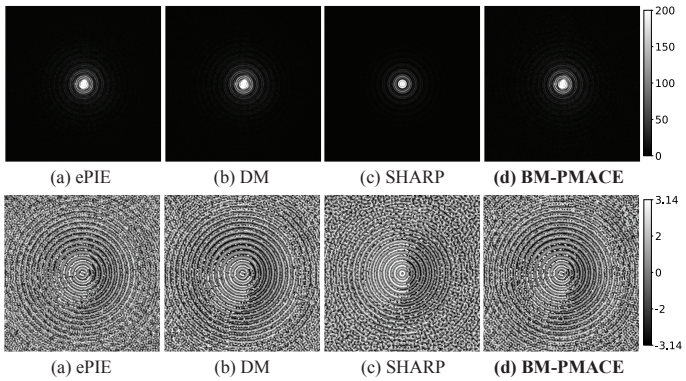

Figure 24: **Single-mode** reconstructions of complex-valued probe from real data. Top: Magnitudes of reconstructed complex probe functions in single-mode reconstruction using ePIE, DM, SHARP, and BM-PMACE. Bottom: Phase (in radians) of the reconstructed complex probe functions.

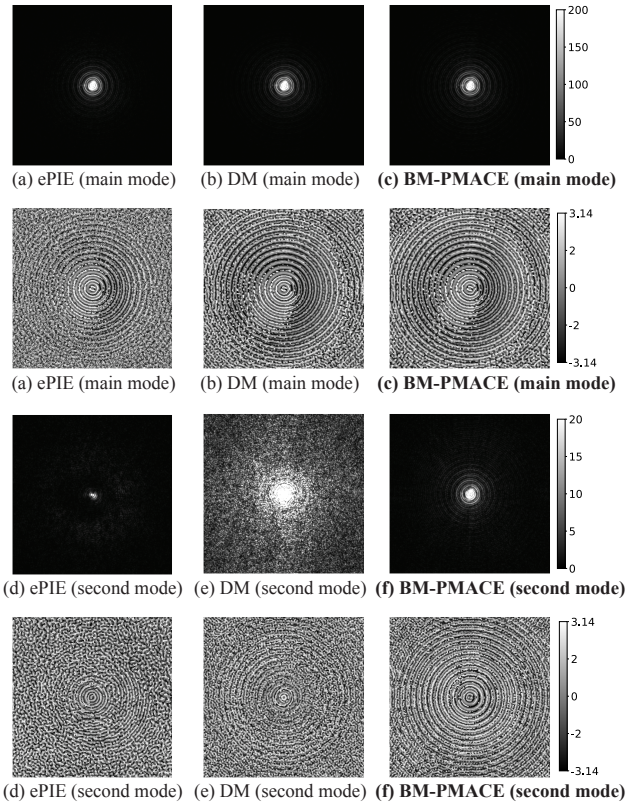

Figure 25: **Two-mode** reconstructions of complex-valued probes from real data. Top row: Magnitudes of the reconstructed complex probe functions for the main mode, using ePIE, DM, SHARP, and BM-PMACE. Second row: Phase (in radians) of the reconstructed complex probe function for the main mode. Third and fourth rows: Magnitudes and phases (in radians) of the reconstructed complex probe function for the secondary mode from measured data. BM-PMACE yields reconstructions with more defined features in both modes.

capture more than 95% of the total energy. However, the secondary mode exhibited notable differences. The secondary mode reconstructed using ePIE has low density and carries subtle phase information, and thus appears dim in Figure 25. The secondary mode reconstructed using DM provides more information but still lacks detail. BM-PMACE produces a secondary mode with more detailed density and phase information, demonstrating its ability to capture complex features in multi-mode reconstructions. We limit our experiment to two probe modes, as adding more modes did not further improve reconstruction quality.

Method	Reconstruction	
	Single-mode	Two-mode
ePIE	0.094	0.087
DM	0.090	0.075
SHARP	0.081	-
BM-PMACE	**0.079**	**0.067**

Table II: Comparison of forward-propagated NRMSE for each reconstruction method under single-mode and two-mode conditions. The ”-” indicates that the reconstruction condition is not supported by the method.

Table II displays the forward-propagated NRMSE values for both single-mode and two-mode cases. BM-PMACE achieves the lowest NRMSE of all of the methods in both the single-mode and two-mode cases, indicating that it fits the measurements most effectively. Notably, all methods show improvement when an extra mode is incorporated into the reconstruction.

VII. Conclusion

In this paper we presented BM-PMACE for blind ptychographic reconstruction. Our method offers a robust, efficient, and flexible framework for accurately estimating complex transmittance images and probe functions, leveraging the benefit of local refinement of probe estimate while maintaining the parallel structure among the agents. Additionally, it accommodates multiple probe modes, which enables effective reconstruction in scenarios with partially coherent illumination.

We applied BM-PMACE to blind ptychography on both synthetic noisy data and measured data. The results indicate that BM-PMACE achieves high-quality reconstruction with fewer iterations compared to existing methods, potentially reducing computational time and resources. Additionally, BM-PMACE exhibited rapid convergence to a stable state, even in the presence of noise in data. Overall, BM-PMACE provides a reliable framework for accurate and efficient ptychographic reconstruction.

References

[1] P. Nellist, B. McCallum, and J. M. Rodenburg, “Resolution beyond the ’information limit’ in transmission electron microscopy,” *Nature*, vol. 374, no. 6523, pp. 630–632, 1995.

[2] J. M. Rodenburg and H. M. Faulkner, “A phase retrieval algorithm for shifting illumination,” *Applied Physics Letters*, vol. 85, no. 20, pp. 4795–4797, 2004.

[3] J. M. Rodenburg, A. Hurst, A. G. Cullis, B. R. Dobson, F. Pfeiffer, O. Bunk, C. David, . f. K. Jefimovs, and I. Johnson, “Hard-x-ray lensless imaging of extended objects,” *Physical Review Letters*, vol. 98, no. 3, p. 034801, 2007.

[4] F. Pfeiffer, "X-ray ptychography," *Nature Photonics*, vol. 12, no. 1, pp. 9–17, 2018.

[5] J. Rodenburg and A. Maiden, "Ptychography," *Springer Handbook of Microscopy*, pp. 819–904, 2019.

[6] P. Li and A. Maiden, "Multi-slice ptychographic tomography," *Scientific Reports*, vol. 8, no. 1, p. 2049, 2018.

[7] D. J. Chang, D. S. Kim, A. Rana, X. Tian, J. Zhou, P. Ercius, and J. Miao, "Ptychographic atomic electron tomography: Towards three-dimensional imaging of individual light atoms in materials," *Physical Review B*, vol. 102, no. 17, p. 174101, 2020.

[8] D. Batey, C. Rau, and S. Cipiccia, "High-speed x-ray ptychographic tomography," *Scientific Reports*, vol. 12, no. 1, p. 7846, 2022.

[9] R. Górecki, C. C. Polo, T. A. Kalile, E. X. Miqueles, Y. R. Tonin, L. Upadhyaya, F. Meneau, and S. P. Nunes, "Ptychographic x-ray computed tomography of porous membranes with nanoscale resolution," *Communications Materials*, vol. 4, no. 1, p. 68, 2023.

[10] P. M. Pelz, S. M. Griffin, S. Stonemeyer, D. Popple, H. DeVyldere, P. Ercius, A. Zettl, M. C. Scott, and C. Ophus, "Solving complex nanostructures with ptychographic atomic electron tomography," *Nature Communications*, vol. 14, no. 1, p. 7906, 2023.

[11] T. Wang, S. Jiang, P. Song, R. Wang, L. Yang, T. Zhang, and G. Zheng, "Optical ptychography for biomedical imaging: recent progress and future directions," *Biomedical Optics Express*, vol. 14, no. 2, pp. 489–532, 2023.

[12] C. Guo, S. Jiang, L. Yang, P. Song, A. Pirhanov, R. Wang, T. Wang, X. Shao, Q. Wu, Y. K. Cho *et al.*, "Depth-multiplexed ptychographic microscopy for high-throughput imaging of stacked bio-specimens on a chip," *Biosensors and Bioelectronics*, vol. 224, p. 115049, 2023.

[13] P. Wang, F. Zhang, S. Gao, M. Zhang, and A. I. Kirkland, "Electron ptychographic diffractive imaging of boron atoms in lab6 crystals," *Scientific Reports*, vol. 7, no. 1, p. 2857, 2017.

[14] S. Jiang, C. Guo, Z. Bian, R. Wang, J. Zhu, P. Song, P. Hu, D. Hu, Z. Zhang, K. Hoshino *et al.*, "Ptychographic sensor for large-scale lensless microbial monitoring with high spatiotemporal resolution," *Biosensors and Bioelectronics*, vol. 196, p. 113699, 2022.

[15] G. Li, H. Zhang, and Y. Han, "4d-stem ptychography for electron-beam-sensitive materials," *ACS Central Science*, vol. 8, no. 12, pp. 1579–1588, 2022.

[16] H. Chang, P. Enfedaque, Y. Lou, and S. Marchesini, "Partially coherent ptychography by gradient decomposition of the probe," *Acta Crystallographica Section A: Foundations and Advances*, vol. 74, no. 3, pp. 157–169, 2018.

[17] H. Chang, L. Yang, and S. Marchesini, "Fast iterative algorithms for blind phase retrieval: A survey," in *Handbook of Mathematical Models and Algorithms in Computer Vision and Imaging: Mathematical Imaging and Vision*. Springer, 2023, pp. 139–174.

[18] A. Pan, C. Zuo, and B. Yao, "High-resolution and large field-of-view fourier ptychographic microscopy and its applications in biomedicine," *Reports on Progress in Physics*, vol. 83, no. 9, p. 096101, 2020.

[19] G. Zheng, C. Shen, S. Jiang, P. Song, and C. Yang, "Concept, implementations and applications of fourier ptychography," *Nature Reviews Physics*, vol. 3, no. 3, pp. 207–223, 2021.

[20] J. Deng, Y. S. Nashed, S. Chen, N. W. Phillips, T. Peterka, R. Ross, S. Vogt, C. Jacobsen, and D. J. Vine, "Continuous motion scan ptychography: characterization for increased speed in coherent x-ray imaging," *Optics Express*, vol. 23, no. 5, pp. 5438–5451, 2015.

[21] H. Chang, P. Enfedaque, and S. Marchesini, "Blind ptychographic phase retrieval via convergent alternating direction method of multipliers," *SIAM Journal on Imaging Sciences*, vol. 12, no. 1, pp. 153–185, 2019.

[22] H. Tamaki and K. Saitoh, "Near-field electron ptychography using full-field structured illumination," *Microscopy*, p. dfae035, 2024.

[23] J. M. Rodenburg, "Ptychography and related diffractive imaging methods," *Advances in Imaging and Electron Physics*, vol. 150, pp. 87–184, 2008.

[24] T. E. Moxham, A. Parsons, T. Zhou, L. Alianelli, H. Wang, D. Laundy, V. Dhamgaye, O. J. Fox, K. Sawhney, and A. M. Korsunsky, "Hard x-ray ptychography for optics characterization using a partially coherent synchrotron source," *Journal of Synchrotron Radiation*, vol. 27, no. 6, pp. 1688–1695, 2020.

[25] Y. Yao, Y. Jiang, J. A. Klug, M. Wojcik, E. R. Maxey, N. S. Sirica, C. Roehrig, Z. Cai, S. Vogt, B. Lai *et al.*, "Multi-beam x-ray ptychography for high-throughput coherent diffraction imaging," *Scientific Reports*, vol. 10, no. 1, p. 19550, 2020.

[26] J. Deng, D. J. Vine, S. Chen, Y. S. Nashed, T. Peterka, R. Ross, S. Vogt, and C. J. Jacobsen, "Opportunities and limitations for combined fly-scan ptychography and fluorescence microscopy," in *X-Ray Nanoimaging: Instruments and Methods II*, vol. 9592. SPIE, 2015, pp. 111–119.

[27] X. Huang, K. Lauer, J. N. Clark, W. Xu, E. Nazaretski, R. Harder, I. K. Robinson, and Y. S. Chu, "Fly-scan ptychography," *Scientific Reports*, vol. 5, no. 1, p. 9074, 2015.

[28] P. M. Pelz, M. Guizar-Sicairos, P. Thibault, I. Johnson, M. Holler, and A. Menzel, "On-the-fly scans for x-ray ptychography," *Applied Physics Letters*, vol. 105, no. 25, 2014.

[29] P. Thibault and A. Menzel, "Reconstructing state mixtures from diffraction measurements," *Nature*, vol. 494, no. 7435, pp. 68–71, 2013.

[30] D. J. Batey, D. Claus, and J. M. Rodenburg, "Information multiplexing in ptychography," *Ultramicroscopy*, vol. 138, pp. 13–21, 2014.

[31] A. Fannjiang and P. Chen, "Blind ptychography: uniqueness and ambiguities," *Inverse Problems*, vol. 36, no. 4, p. 045005, 2020.

[32] R. Hesse, D. R. Luke, S. Sabach, and M. K. Tam, "Proximal heterogeneous block implicit-explicit method and application to blind ptychographic diffraction imaging," *SIAM Journal on Imaging Sciences*, vol. 8, no. 1, pp. 426–457, 2015.

[33] A. Maiden, D. Johnson, and P. Li, "Further improvements to the ptychographical iterative engine," *Optica*, vol. 4, no. 7, pp. 736–745, 2017.

[34] X. Long, L. Rong, H. Lin, Y. Wang, J. Zhao, S. Lin, and D. Wang, "Single-shot ptychography based on spatial light modulator multi-angle modulation," in *Thirteenth International Conference on Information Optics and Photonics (CIOP 2022)*, vol. 12478. SPIE, 2022, pp. 909–918.

[35] V. Elser, "Phase retrieval by iterated projections," *JOSA A*, vol. 20, no. 1, pp. 40–55, 2003.

[36] Z. Dong, Y.-L. L. Fang, X. Huang, H. Yan, S. Ha, W. Xu, Y. S. Chu, S. I. Campbell, and M. Lin, "High-performance multi-mode ptychography reconstruction on distributed gpus," in *2018 New York Scientific Data Summit (NYSDS)*. IEEE, 2018, pp. 1–5.

[37] S. Marchesini, H. Krishnan, B. J. Daurer, D. A. Shapiro, T. Perciano, J. A. Sethian, and F. R. Maia, "SHARP: a distributed GPU-based ptychographic solver," *Journal of Applied Crystallography*, vol. 49, no. 4, pp. 1245–1252, 2016.

[38] R. Xu, M. Soltanolkotabi, J. P. Haldar, W. Unglaub, J. Zusman, A. F. Levi, and R. M. Leahy, "Accelerated Wirtinger flow: A fast algorithm for ptychography," *arXiv preprint arXiv:1806.05546*, 2018.

[39] P. Enfedaque, H. Chang, B. Enders, D. Shapiro, and S. Marchesini, "High performance partial coherent x-ray ptychography," in *Computational Science–ICCS 2019*. Springer, Jun. 2019, pp. 46–59.

[40] Q. Zhai, G. T. Buzzard, K. Mertes, B. Wohlberg, and C. A. Bouman, "Projected multi-agent consensus equilibrium (PMACE) with application to ptychography," *IEEE Transactions on Computational Imaging*, 2023.

[41] H. M. L. Faulkner and J. Rodenburg, "Movable aperture lensless transmission microscopy: a novel phase retrieval algorithm," *Physical Review Letters*, vol. 93, no. 2, p. 023903, 2004.

[42] A. M. Maiden and J. M. Rodenburg, "An improved ptychographical phase retrieval algorithm for diffractive imaging," *Ultramicroscopy*, vol. 109, no. 10, pp. 1256–1262, 2009.

[43] A. M. Maiden, M. J. Humphry, and J. M. Rodenburg, "Ptychographic transmission microscopy in three dimensions using a multi-slice approach," *JOSA A*, vol. 29, no. 8, pp. 1606–1614, 2012.

[44] P. Thibault, M. Dierolf, A. Menzel, O. Bunk, C. David, and F. Pfeiffer, "High-resolution scanning x-ray diffraction microscopy," *Science*, vol. 321, no. 5887, pp. 379–382, 2008.

[45] P. Thibault, M. Dierolf, O. Bunk, A. Menzel, and F. Pfeiffer, "Probe retrieval in ptychographic coherent diffractive imaging," *Ultramicroscopy*, vol. 109, no. 4, pp. 338–343, 2009.

[46] S. Marchesini, A. Schirotzek, C. Yang, H.-t. Wu, and F. Maia, "Augmented projections for ptychographic imaging," *Inverse Problems*, vol. 29, no. 11, p. 115009, 2013.

[47] Y. Yao, Y. Jiang, J. Klug, Y. Nashed, C. Roehrig, C. Preissner, F. Marin, M. Wojcik, O. Cossairt, Z. Cai *et al.*, "Broadband x-ray ptychography using multi-wavelength algorithm," *Journal of Synchrotron Radiation*, vol. 28, no. 1, pp. 309–317, 2021.

[48] X. Shi, N. Burdet, D. Batey, and I. Robinson, "Multi-modal ptychography: Recent developments and applications," *Applied Sciences*, vol. 8, no. 7, p. 1054, 2018.

[49] Y.-L. L. Fang, S. Ha, X. Huang, H. Yan, Z. Dong, Y. S. Chu, S. I. Campbell, W. Xu, and M. Lin, "Accelerated computing for x-ray ptychography at nsls-ii," in *Handbook on Big Data and Machine Learning in the Physical Sciences: Volume 2. Advanced Analysis Solutions for Leading Experimental Techniques*. World Scientific, 2020, pp. 141–157.

[50] X. Yu, V. Nikitin, D. J. Ching, S. Aslan, D. Gürsoy, and T. Biçer, "Scalable and accurate multi-GPU-based image reconstruction of large-scale ptychography data," *Scientific Reports*, vol. 12, no. 1, p. 5334, 2022.

[51] O. Bunk, M. Dierolf, S. Kynde, I. Johnson, O. Marti, and F. Pfeiffer, "Influence of the overlap parameter on the convergence of the ptychographical iterative engine," *Ultramicroscopy*, vol. 108, no. 5, pp. 481–487, 2008.

[52] O. Melnyk, "Convergence properties of gradient methods for blind ptychography," *arXiv preprint arXiv:2306.08750*, 2023.

[53] M. Odstrčil, A. Menzel, and M. Guizar-Sicairos, "Iterative least-squares solver for generalized maximum-likelihood ptychography," *Optics express*, vol. 26, no. 3, pp. 3108–3123, 2018, code available at `https://www.psi.ch/en/sls/csaxs/software`

[54] T. Aidukas, N. W. Phillips, A. Diaz, E. Poghosyan, E. Müller, A. F. Levi, G. Aeppli, M. Guizar-Sicairos, and M. Holler, "High-performance 4-nm-resolution x-ray tomography using burst ptychography," *Nature*, vol. 632, no. 8023, pp. 81–88, 2024.

[55] K. Wakonig, H.-C. Stadler, M. Odstrčil, E. H. Tsai, A. Diaz, M. Holler, I. Usov, J. Raabe, A. Menzel, and M. Guizar-Sicairos, "Ptychoshelves, a versatile high-level framework for high-performance analysis of ptychographic data," *Applied Crystallography*, vol. 53, no. 2, pp. 574–586, 2020.

[56] M. Du, H. Ruth, S. Henke, A. Tripathi, and V. Nikitin, "Advancedphotonsource/pty-chi: v1.2.0," 2025. [Online]. Available: https://zenodo.org/record/16104408

[57] S. Kandel, S. Maddali, M. Allain, S. O. Hruszkewycz, C. Jacobsen, and Y. S. Nashed, "Using automatic differentiation as a general framework for ptychographic reconstruction," *Optics express*, vol. 27, no. 13, pp. 18 653–18 672, 2019.

[58] L. Wu, S. Yoo, Y. S. Chu, X. Huang, and I. K. Robinson, "Dose-efficient automatic differentiation for ptychographic reconstruction," *Optica*, vol. 11, no. 6, pp. 821–830, 2024.

[59] Y. Shao, S. Weerdenburg, J. Seifert, H. P. Urbach, A. P. Mosk, and W. Coene, "Wavelength-multiplexed multi-mode euv reflection ptychography based on automatic differentiation," *Light: Science & Applications*, vol. 13, no. 1, p. 196, 2024.

[60] X. Jiang, G. J. Gang, and J. W. Stayman, "Ctorch: Pytorch-compatible gpu-accelerated auto-differentiable projector toolbox for computed tomography," *arXiv preprint arXiv:2503.16741*, 2025.

[61] M. Blondel, Q. Berthet, M. Cuturi, R. Frostig, S. Hoyer, F. Llinares-López, F. Pedregosa, and J.-P. Vert, "Efficient and modular implicit differentiation," *Advances in Neural Information Processing Systems*, vol. 35, pp. 5230–5242, 2022.

[62] F. Guzzi, A. Gianoncelli, F. Billè, S. Carrato, and G. Kourousias, "Automatic differentiation for inverse problems in x-ray imaging and microscopy," *Life*, vol. 13, no. 3, p. 629, 2023.

[63] J. Hueckelheim, H. Menon, W. S. Moses, B. Christianson, P. Hovland, and L. Hascoet, "A short review of automatic differentiation pitfalls in scientific computing," in *ICML 2023 Workshop on Differentiable Almost Everything: Differentiable Relaxations, Algorithms, Operators, and Simulators*, 2023.

[64] Y. S. Nashed, D. J. Vine, T. Peterka, J. Deng, R. Ross, and C. Jacobsen, "Parallel ptychographic reconstruction," *Optics Express*, vol. 22, no. 26, pp. 32 082–32 097, 2014.

[65] M. Odstrcil, P. Baksh, S. Boden, R. Card, J. Chad, J. Frey, and W. Brocklesby, "Ptychographic coherent diffractive imaging with orthogonal probe relaxation," *Optics express*, vol. 24, no. 8, pp. 8360–8369, 2016.

[66] Z. Chen, M. Odstrcil, Y. Jiang, Y. Han, M.-H. Chiu, L.-J. Li, and D. A. Muller, "Mixed-state electron ptychography enables sub-angstrom resolution imaging with picometer precision at low dose," *Nature communications*, vol. 11, no. 1, p. 2994, 2020.

[67] Q. Zhai, B. Wohlberg, G. T. Buzzard, and C. A. Bouman, "Projected multi-agent consensus equilibrium for ptychographic image reconstruction," in *2021 55th Asilomar Conference on Signals, Systems, and Computers*. IEEE, 2021, pp. 1694–1698.

[68] L. Bian, J. Suo, J. Chung, X. Ou, C. Yang, F. Chen, and Q. Dai, "Fourier ptychographic reconstruction using poisson maximum likelihood and truncated Wirtinger gradient," *Scientific Reports*, vol. 6, no. 1, p. 27384, 2016.

[69] P. Godard, M. Allain, V. Chamard, and J. Rodenburg, "Noise models for low counting rate coherent diffraction imaging," *Optics Express*, vol. 20, no. 23, pp. 25 914–25 934, 2012.

[70] S. Marchesini, "Ptychography gold ball example dataset," 7 2017. [Online]. Available: https://www.osti.gov/biblio/1454414

VIII. Biography Section

Qiuchen Zhai (Student Member, IEEE) received the B.S. degree in electronic information engineering from the University of Electronic Science and Technology of China (UESTC), Chengdu, China, in 2018, and the M.S. degree in electrical and computer engineering from The Ohio State University, Columbus, OH, USA, in 2019. She earned her Ph.D. in Electrical and Computer Engineering from Purdue University, West Lafayette, IN, USA, in 2024. Her research interests include signal and image processing, computational imaging, inverse problems, and machine learning.

Gregery T. Buzzard (Senior Member, IEEE) is Professor of Mathematics at Purdue University, where he served as Department Head for 7 years. He has a PhD from the University of Michigan and held postdoctoral appointments at Indiana University and Cornell University before joining Purdue. His research has led to theoretical advances in dynamical systems and experiment design and to new algorithms for image and volume reconstruction for a variety of sensing modalities. The unifying ideas in his recent work are iterative methods for image reconstruction and reduction of uncertainty through appropriate measurement schemes.

Kevin M. Mertes is a scientist at Los Alamos National Laboratory. He earned is PhD from City University Of New York. He has conducted experimental research in quantum tunneling of magnetization in single molecule magnets, the metal-insulator transition in 2D electron gases and the mixing dynamics of spinor Bose-Einstein condensates. He has also conducted experimental and computational work in hyper-spectral remote sensing and x-ray ptychography.

Brendt Wohlberg (Fellow, IEEE) is a Staff Scientist with Theoretical Division at Los Alamos National Laboratory. He received the B.Sc. (Hons.) degree in applied mathematics, and the M.Sc. (Applied Science) and Ph.D. degrees in electrical engineering from the University of Cape Town, Cape Town, South Africa. He was the Chair of the Computational Imaging Special Interest Group (now the Computational Imaging Technical Committee) of the IEEE Signal Processing Society and was the Editor-in-Chief of the *IEEE Transactions on Computational Imaging*. He is currently Editor-in-Chief of the *IEEE Open Journal of Signal Processing* and is a Fellow of IEEE.

Charles A. Bouman (Fellow, IEEE) is the Showalter Professor of Electrical and Computer Engineering and Biomedical Engineering at Purdue University. He received his B.S.E.E. degree from the University of Pennsylvania, M.S. degree from the University of California at Berkeley, and Ph.D. from Princeton University. He is a member of the National Academy of Inventors as well as a Fellow of IEEE, AIMBE, IS&T, and SPIE. He has served as the IEEE Signal Processing Society's Vice President of Technical Directions as well as the Editor-in-Chief of the *IEEE Transactions on Image Processing*.